Electronic Supplementary Material (ESI) for Journal of Materials Chemistry A.

Electronic supplementary information

Hole dynamic acceleration over CdSO nanoparticles for high-efficiency solar hydrogen production with urea photolysis

Fengting Luo,[a,b] Wen Qiao,[a] Huichao He,[c] Xiaoyong Xu,*[,a,b] Jingguo Hu,*[,b] Yong Zhou*[,d] and Dunhui Wang,*[,a,d]

---

[a] *College of Electronics and Information, Hangzhou Dianzi University, Hangzhou 310018, China. E-mail: xxy@yzu.edu.cn and wangdh@nju.edu.cn*

[b] *College of Physics Science and Technology, Yangzhou University, Yangzhou 225002, China. E-mail: jghu@yzu.edu.cn*

[c] *State Key Laboratory of Environmental Friendly Energy Materials, Southwest University of Science and Technology, Mianyang 621010, China. E-mail: hehuichao@swust.edu.cn*

[d] *School of Physics, Nanjing University, Nanjing 210093, China. E-mail: zhouyong1999@nju.edu.cn*

Sections Page

Note S1. Calculation method for depletion layer width

The diffusion lengths of electron and hole are two important parameters for evaluating the charge transport property in semiconductors. The charge separation mechanism depends on the relative magnitude between crystal size and depletion layer width (W).[1] Thus the W in CdS_xO sample was estimated according to the following equation[2]

$$W=\sqrt{\frac{2\varepsilon_0\varepsilon\left(V-V_F\right)}{\mathrm{e}N_d}} \tag{E1}$$

where ε_0 is the vacuum dielectric constant, ε is the relative dielectric constant (~5.4 for CdS),[3] e is the electron charge (1.6×10^{-19} C), V_F, N_d are the flat potential and the carrier concentration, which are taken as -0.18 V vs. RHE and 1.18×10^{25} m^{-3} according to the Mott-Schottky data (Supplementary Fig. 19). The estimated W at ca. 6.2 nm is close to the mean grain size obtained from XRD and HR-TEM results (Supplementary Fig. 1 and Fig. 1c) , meaning the absence of space charge field with the essentially flat energy bands in nanograins. In addition, the grains exceed the quantum-confined space defined by the Bohr exciton radius (R_{B} ~ 3 nm).[3] Thus the charge separation is driven mainly by free diffusion in small grains, enabling the surface-reaching propensities for both types of charge carriers.

Note S2. Calculation method for apparent quantum yield (AQY)

The AQY values were calculated by the following equation:[4]

$$\begin{aligned}\text{AQY [\%]} &= \frac{\text{number of reacted electrons}}{\text{number of incident photons}} \times 100\% \\ &= \frac{\text{number of evolved } \mathrm{H_2} \text{ molecules} \times 2}{\text{number of incident photons}} \times 100\% \\ &= \frac{M_{\mathrm{H_2}} \times N_{\mathrm{A}} \times 2 \times h \times c}{I_{\mathrm{i}} \times S \times t \times \lambda} \times 100\%\end{aligned} \tag{E2}$$

where $M_{\mathrm{H_2}}$ is the mole number of evolved H_2, N_{A}, h are the Avogadro's and Planck's constants, c, λ, t, S and I_{i} are the wave speed, wavelength, time, area, and intensity of light irradiation, respectively. I_{i} was determined by FZ-A spectroradiometer (Perfectlight, Beijing) and S was calibrated to be 10 $\mathrm{cm^2}$.

Table S1. Various parameters for AQY calculation.

Wavelength (nm)	Intensity (mW $\mathrm{cm^{-2}}$)	H_2 amount (µmol $\mathrm{h^{-1}}$)
400 (±5 nm)	2	4.31
420 (±5 nm)	1.5	2.27

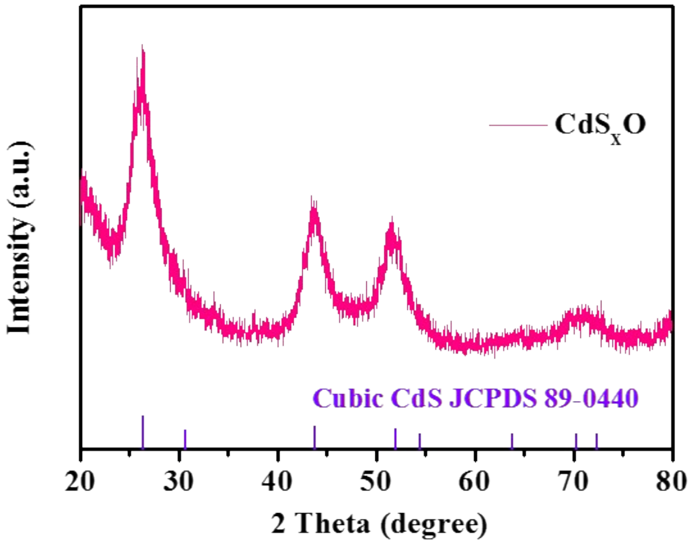

Fig. S1 XRD pattern of as-synthesized CdS$_x$O NPs.

The XRD pattern of as-synthesized CdS$_x$O NPs can be indexed to cubic-phase CdS (JCPDS Card No. 89-0440), and their mean size is estimated using Debye-Scherrer equation as follows:[5]

$$D = 0.89\lambda / \beta \cos\theta_B , \tag{E3}$$

where λ is the x-ray wavelength (0.154 nm), β is the peak width at half maximum and θ_B is the Bragg diffraction angle. Based on overriding (111) peak, the average crystallite size is estimated at approximately 6.5 nm, which is consistent with their HR-TEM observation.

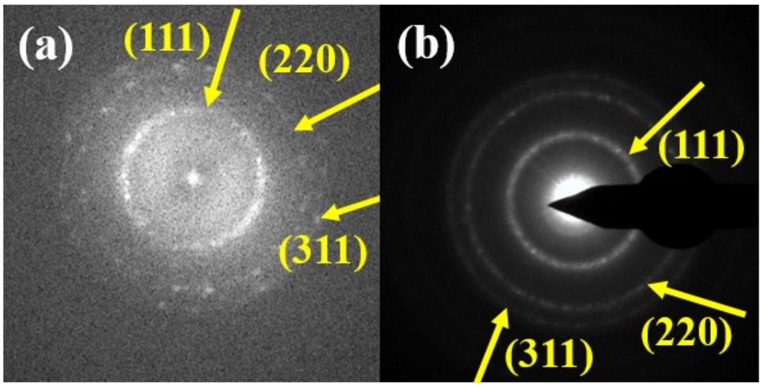

Fig. S2 (a) FFT and (b) SAED patterns of as-synthesized CdS_xO NPs.

Along with XRD and HR-TEM results, the SAED and FFT patterns confirm cubic-phase Cd-S crystallinity in CdS_xO NPs.

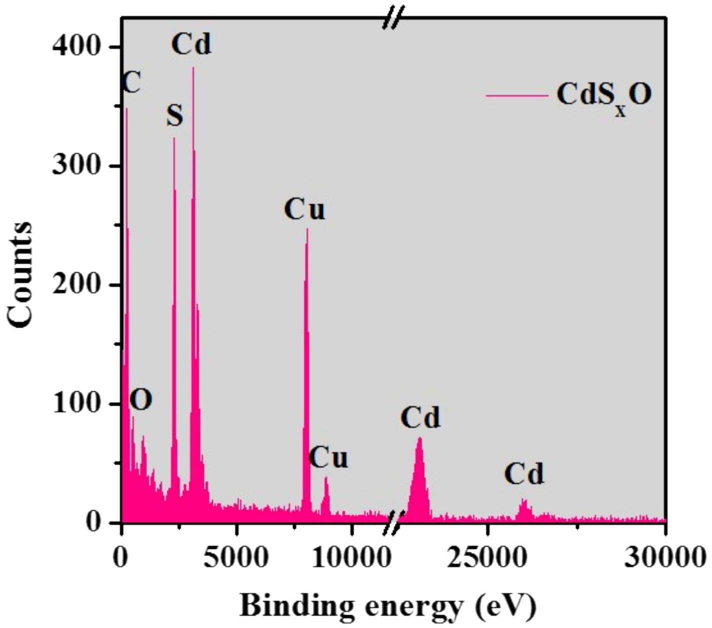

Fig. S3 EDX spectrum of as-synthesized CdS$_x$O NPs.

The EDX analysis reveals the composition of Cd, S, and O elements in CdS$_x$O NPs, besides Cu element from the TEM test bracket.

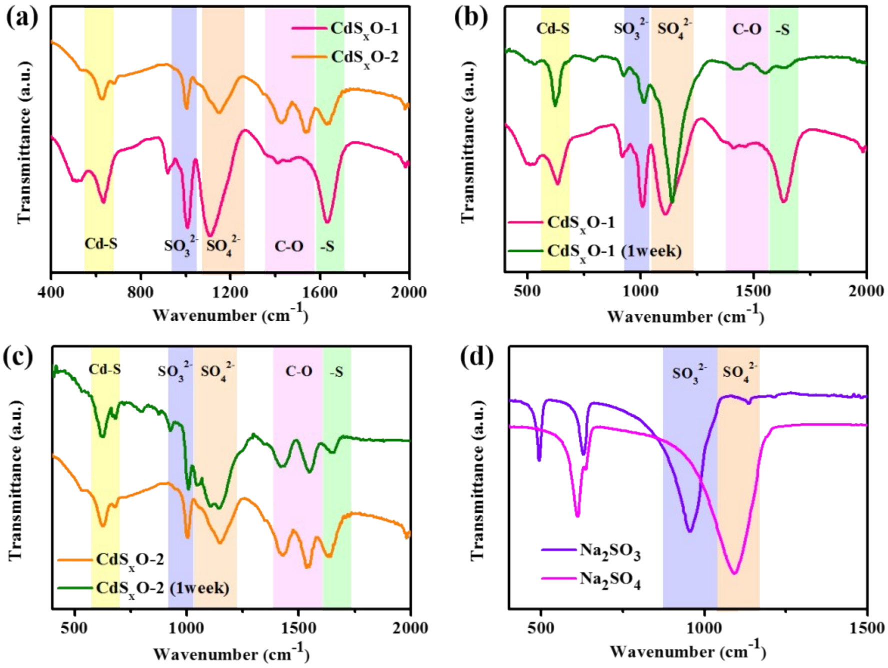

Fig. S4 (a-c) FT-IR spectra of CdS$_x$O-1 and CdS$_x$O-2 with different contents of sulfureous groups before and after roasted at 80 ℃ in air for 1 week. (d) FT-IR spectra of Na_2SO_3 and Na_2SO_4 for identifying characteristic peaks of SO_3^{2-} and SO_4^{2-} groups.

We regulated the atom ratio of Cd to S sources in the reaction mixture to obtain a series of CdS$_x$O samples with different contents of sulfureous groups samples. Two typical representatives synthesized at Cd : S ratios of 1 : 910 and 1 : 1 were labeled CdS$_x$O-1 and CdS$_x$O-2, respectively, and their surface components before and after roasted at 80 ℃ in air for 1 week were probed via the FT-IR spectroscopy. It can be seen that the CdS$_x$O-1 has much more surface sulfureous groups than that of CdS$_x$O-2; moreover those underoxidized –S and SO_3^{2-} molecules would occur oxidation transformation to SO_4^{2-} molecules with roasting time in air. The FT-IR spectra of Na_2SO_3 and Na_2SO_4 can assist to identify the characteristic peaks of SO_3^{2-} and SO_4^{2-} groups.

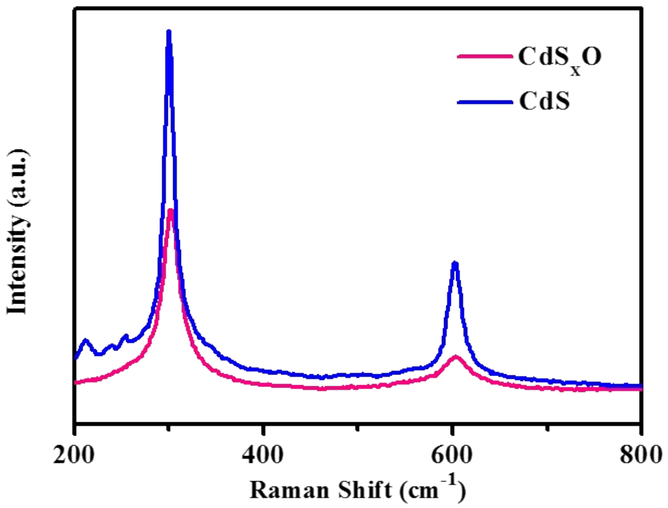

Fig. S5 Raman spectra of CdS$_x$O and pure CdS.

The Raman spectra show two typical peaks at 299 and 600 cm^{-1} of cubic-phase CdS, but the peak intensities of CdS$_x$O sample are much lower than that of pure CdS sample probably due to the shielding effect of massive surface groups.

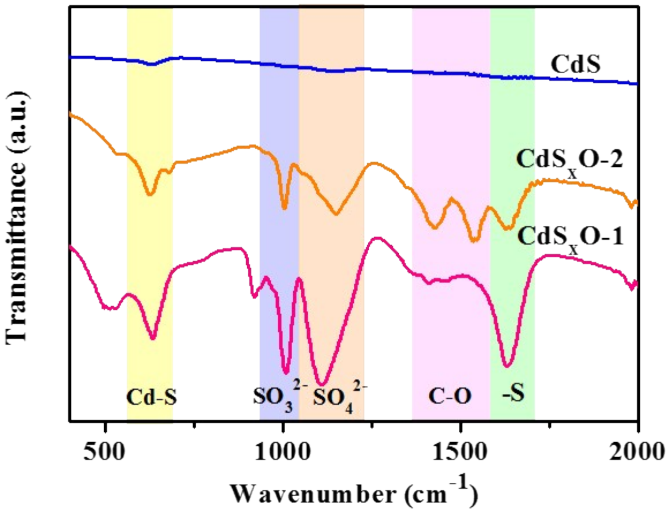

Fig. S6 FT-IR spectra of CdS$_x$O-1 and CdS$_x$O-2 and annealed CdS samples.

The CdS$_x$O-2 sample synthesized in the absence of sulfur-rich environment displays an obvious decline in sulfureous groups compared with CdS$_x$O-1 sample, and moreover the annealed CdS sample almost disappears all FT-IR signals of surface groups due to the removal of sulfureous groups by annealing at 550 ℃.

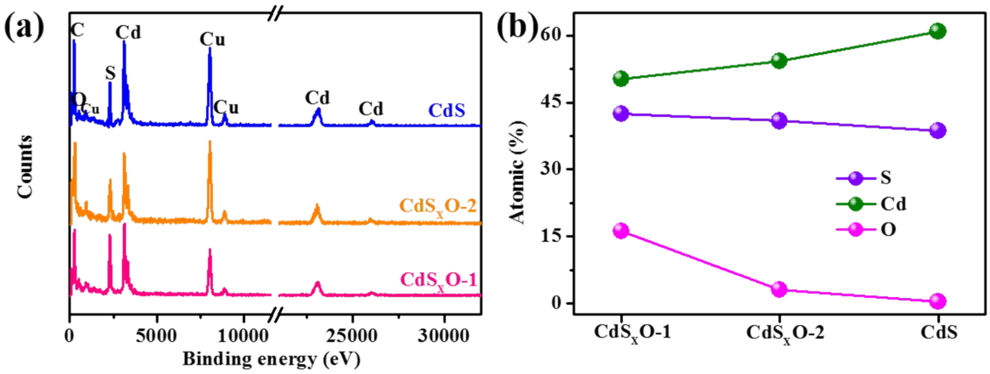

Fig. S7 (a) EDS spectra and (b) corresponding elemental proportions of CdS_xO-1, CdS_xO-2 and annealed CdS samples.

Although it is difficult to determine the exact element proportions in samples since the EDS spectral responsiveness of different elements is different. However, the comparison for element proportions of different samples can provide qualitative insights into change in element composition. Here, the EDS analyses show the maximum proportions of S and O elements and the minimum one of Cd element appear in CdS_xO-1 sample, indicating the surface occupation of sulfureous groups resulted from the sulfur-rich environment.

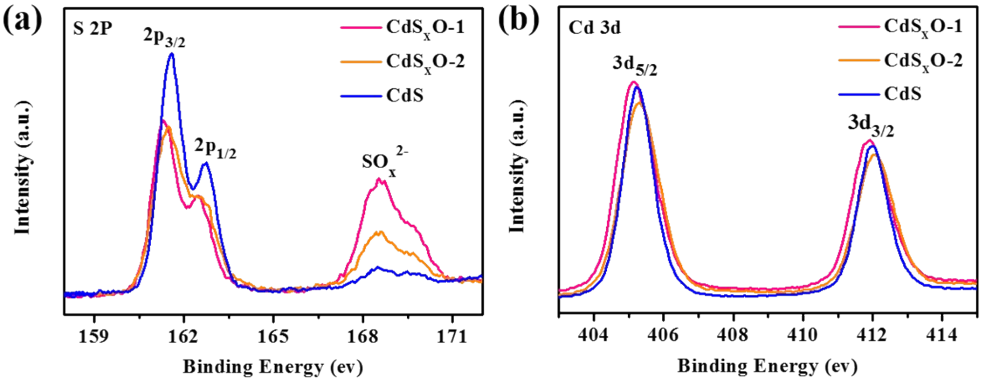

Fig. S8 (a) S 2p and (b) Cd 3d XPS spectra of CdS$_x$O-1, CdS$_x$O-2 and annealed CdS samples.

The XPS spectra exhibit the characteristic peaks of S 2p and Cd 3d in the Cd-S coordination for all samples, but contrast to pure CdS sample, two CdS$_x$O samples especially emerge an obviously asymmetric peak near 169 eV, referring to SO_3^{2-} /SO_4^{2-} molecules, which provides an evidence for the coupling SO_x^{2-} groups.

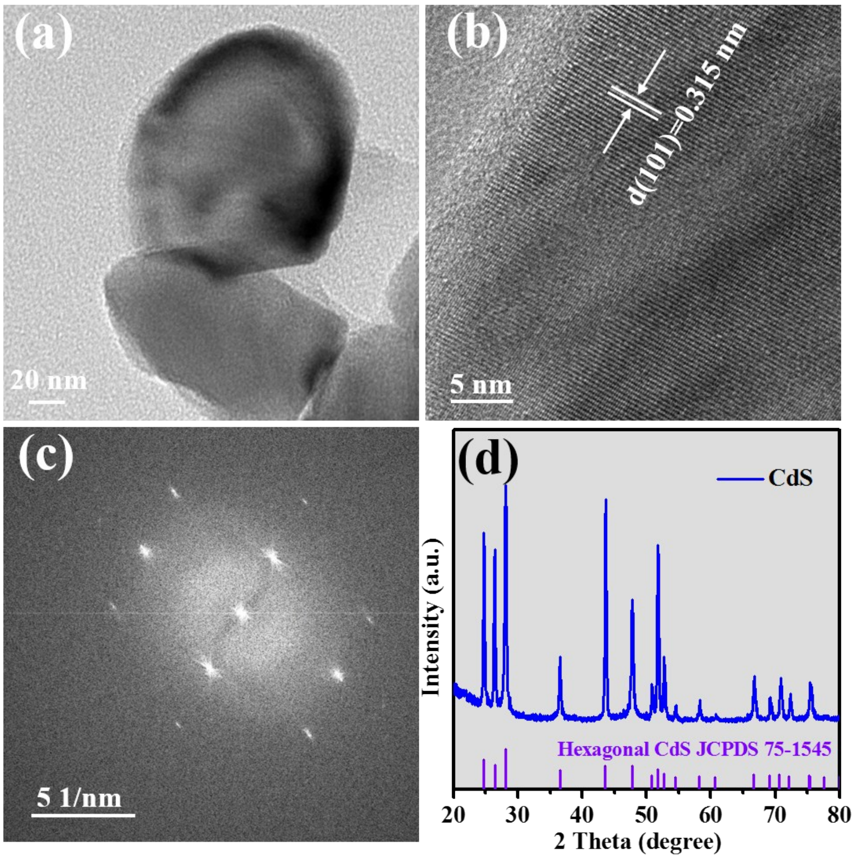

Fig. S9 (a) TEM image, (b) HR-TEM image, (c) FFT and (d) XRD patterns of annealed CdS samples.

During annealing recrystallization, the CdS_xO NPs transform into the larger CdS particles (~ 125 nm) with removal of surface sulfureous groups. The XRD, HR-TEM, and corresponding FFT characterizations together identify the well-defined hexagonal-phase CdS crystallization. Moreover, the mean particle size estimated by Scherrer equation ($D = 0.89\lambda / \beta \cos\theta_B$) is around 130 nm, which accords with the TEM observation.

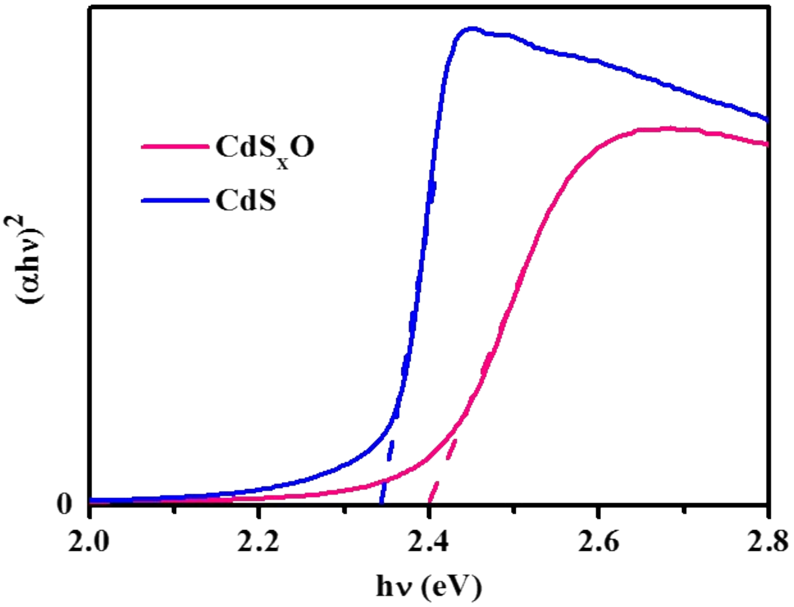

Fig. S10 Tauc plots converted from the absorption spectra of CdS$_x$O and CdS.

The bandgap of CdS$_x$O is estimated to be about 2.4 eV using UV-vis absorption spectrum, which is slightly larger than the bandgap of annealed CdS, probably due to its composition of smaller CdS crystal grains with quantum size effect in CdS$_x$O sample.

.

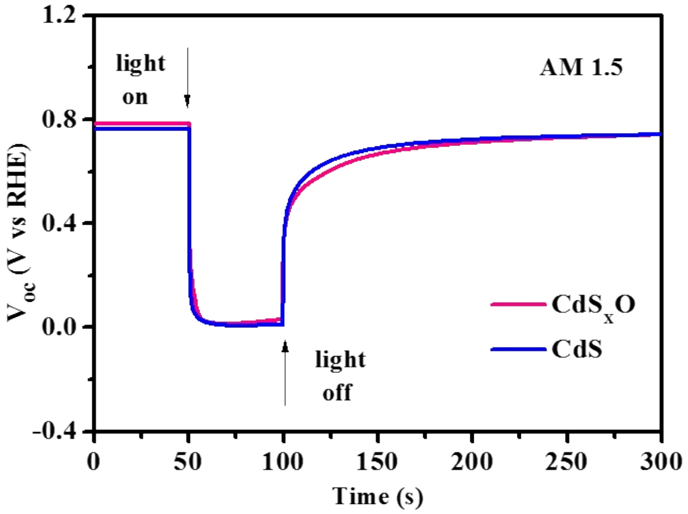

Fig. S11 Time dependence of V_{oc} with ON/OFF switched light irradiation for CdS_xO and CdS.

Upon illumination termination, an evidently slower V_{oc} decay rate is found for CdS_xO sample, reflecting the delaying kinetic of charge recombination in CdS_xO relative to CdS.

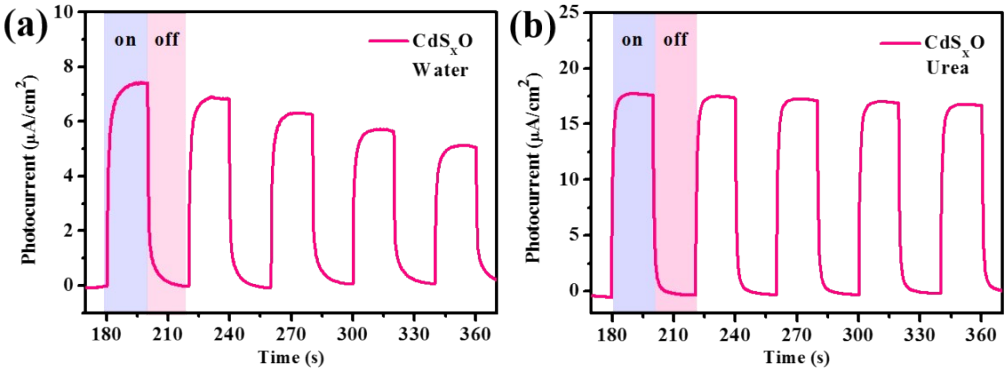

Fig. S12 Time-dependent photocurrents for CdS$_x$O in (a) pure water and (b) urea solution with ON/OFF switched light irradiation.

The time-dependent photocurrent of CdS$_x$O in pure water presents the decaying response signals, which corresponds to the disassembly of sulfureous groups with hole capture agglomeration. However, introducing UOR with low thermodynamic potential as the ultimate destination for photogenerated holes can make the surface sulfureous groups durable mediators for hole transfer, enabling the robust photocurrent response in CdS$_x$O.

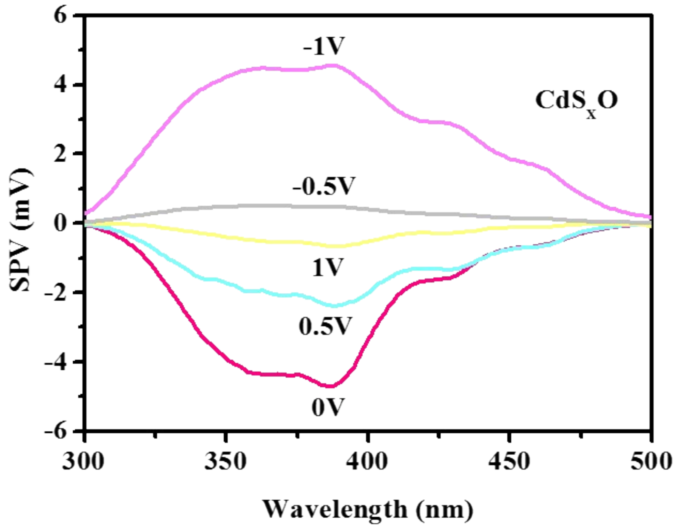

Fig. S13 Bias voltage-dependent SPV spectra for CdS$_x$O.

The bias voltage-dependent SPV spectra show the abnormal change of SPV response intensity with the forward bias increasing, which can be associated with the disassembly of surface sulfureous groups upon hole capture agglomeration.

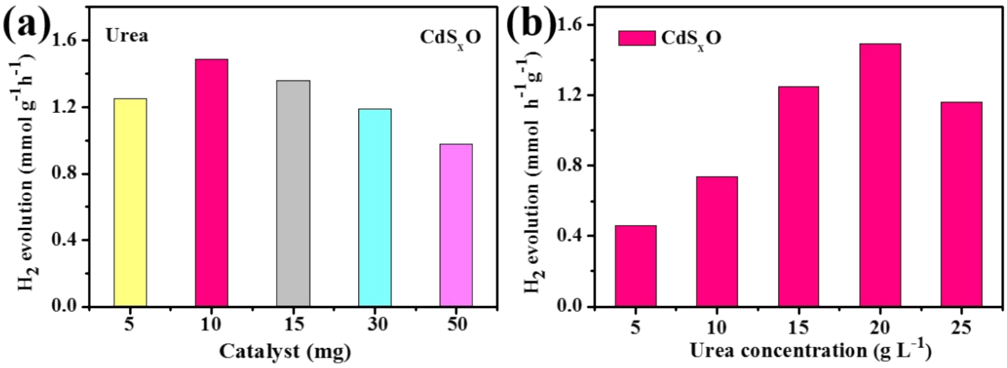

Fig. S14 Comparisons of H_2-evolution activities for CdS$_x$O catalysts with (a) different use dosages and (b) different urea-concentration solutions for optimum photocatalytic conditions.

Based on the photocatalytic performance maximum, the dosages of catalyst and urea were pre-optimized at 0.1 g L^{-1} and 20 g L^{-1}, respectively.

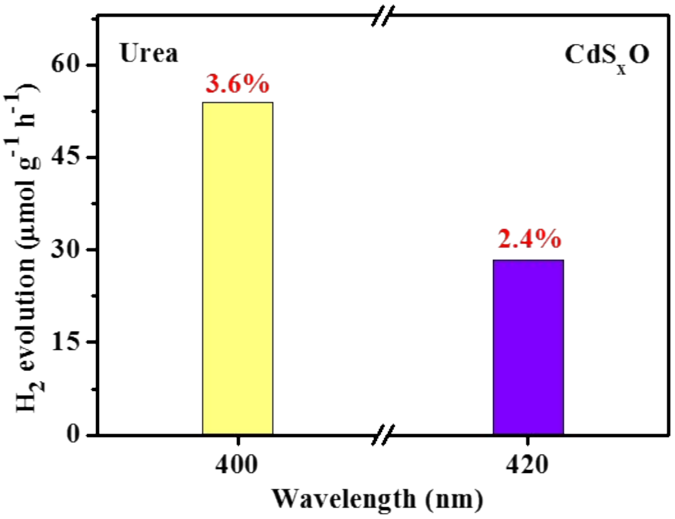

Fig. S15 H_2-evolution rates and AQYs over CdS_xO under the monochromatic light irradiations of 400 and 420 nm, respectively.

The AQYs for the optimum H_2 evolution over CdS_xO coupled with UOR reaches 3.6% at 400 nm and 2.4% at 420 nm without an external electron supply, which is an order of magnitude higher than general efficiency (0.5–1%) reported to date (Supplementary Table 2)[6-9] and even comparable to activity levels with sacrificial agents[10-12].

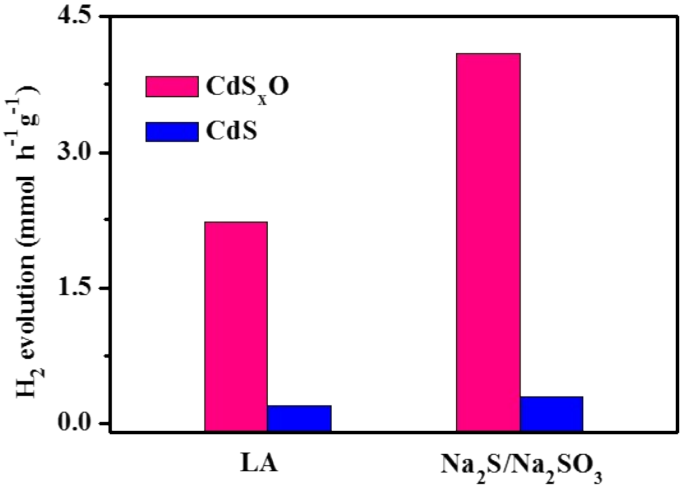

Fig. S16. Comparison of H_2 evolution activities for CdS$_x$O catalysts with using Na_2S/Na_2SO_3 and LA as hole sacrificial agents.

When with using Na_2S/Na_2SO_3 or lactic acid (LA) as hole sacrificial agents, the pure CdS only displays a little bit of activity, whereas the CdS$_x$O renders an outstanding activity growth. This proves an important role of surface sulfureous groups in modulating charge transfer and separation, which especially cannot be imitated by dissociative sulfureous ions in Na_2S/Na_2SO_3 solution.

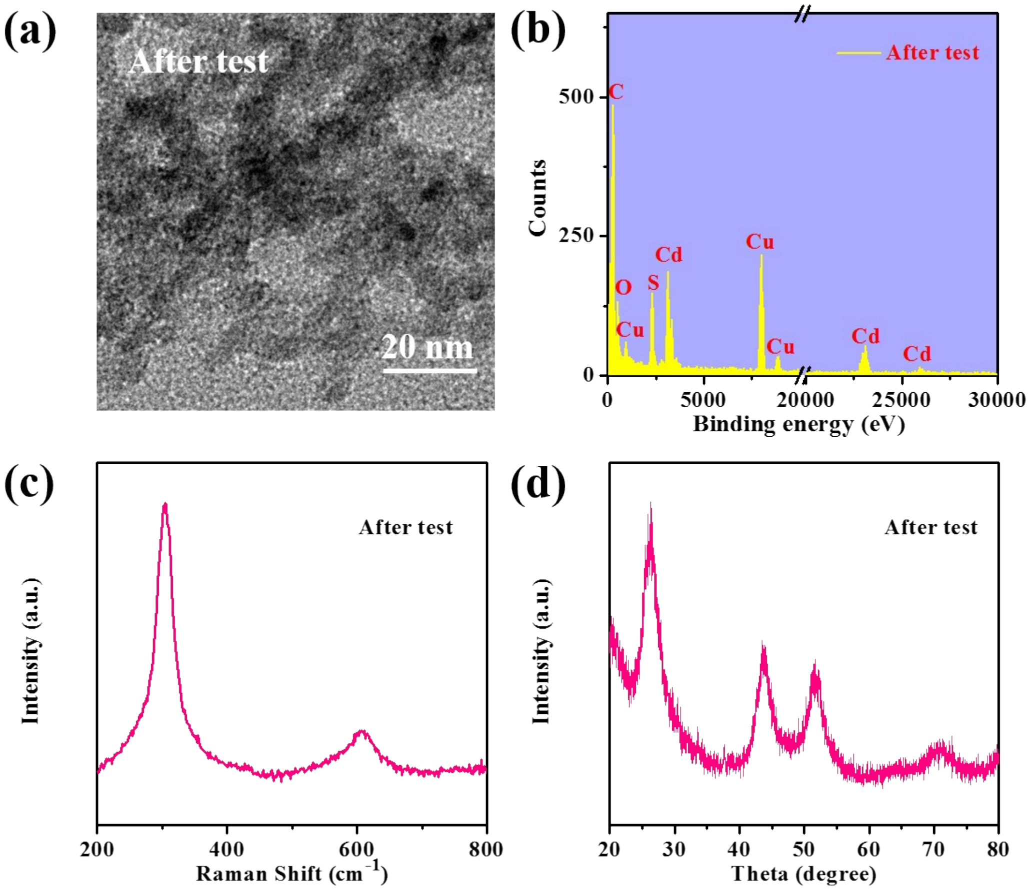

Fig. S17 (a) TEM image, (b) EDX spectrum, (c) Raman spectrum and (d) XRD pattern of CdS_xO catalyst after stability testing.

The microstructure characterizations for CdS_xO catalyst after stability testing together show no noticeable change compared with those before use, confirming the excellent stability of CdS_xO catalyst during photocatalytic process.

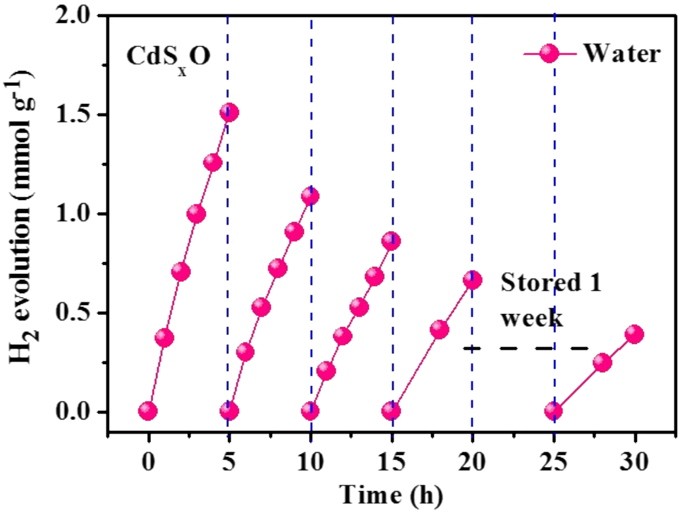

Fig. S18 H_2-evolution stability in cycling runs for CdS$_x$O catalyst in pure water without any sacrifice agents.

The activity decay is observed for cycling H_2 evolution over CdS$_x$O in pure water without urea, implying the disassembly of sulfureous groups under hole accumulation. By contrast, the introduction of amiable UOR can make surface sulfureous groups from self-harm collector to self-healing mediator with hole transfer acceleration.

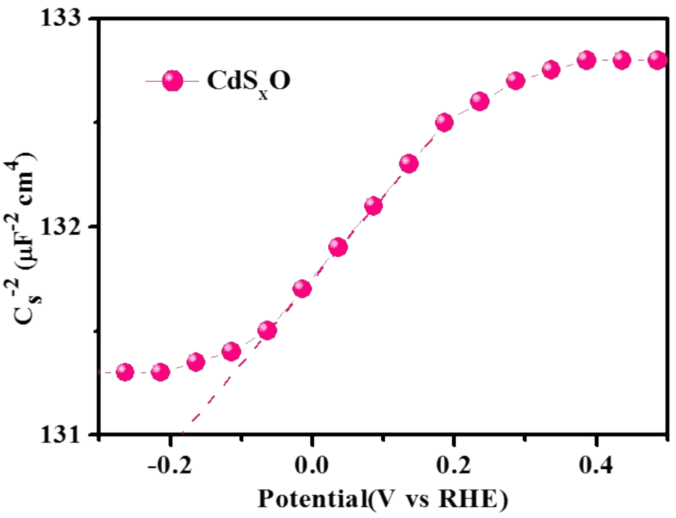

Fig. S19 Mott–Schottky plot for CdS$_x$O sample in dark.

The capacitance measurement at solid-liquid interface was employed to estimate the flatband potential (E_{fb}) using Mott-Schottky plots with $1/C_{\mathrm{sc}}{}^2$ versus potential at a fixed frequency of 100 kHz in dark. The E_{fb} can be obtained by the Mott-Schottky plots based on the following equation:

$$1/C_{\mathrm{sc}}{}^2 = 2(E_{\mathrm{a}} - E_{\mathrm{fb}} - \kappa T/\mathrm{e})/(\mathrm{e}N\varepsilon_0\varepsilon_{\mathrm{s}}A^2) \qquad \text{(S4)}$$

where C_{sc} is the space charge capacity, E_{a} is the applied potential, E_{fb} is the flat band potential and can be determined by extrapolation to a capacitance of zero, κ is the Boltzmann constant, T is the absolute temperature, e is the electron charge, N is the carrier density, ε_{s} is the dielectric constant of materials, ε_0 is the electric permittivity of free space, and A is the area of electrode. E_{fb} can be determined at ca. -0.18 V vs. RHE by extrapolation to a capacitance of zero. The bandgap of CdS$_x$O is estimated to be about 2.4 eV using UV-vis absorption spectrum in Supplementary Fig. 10.

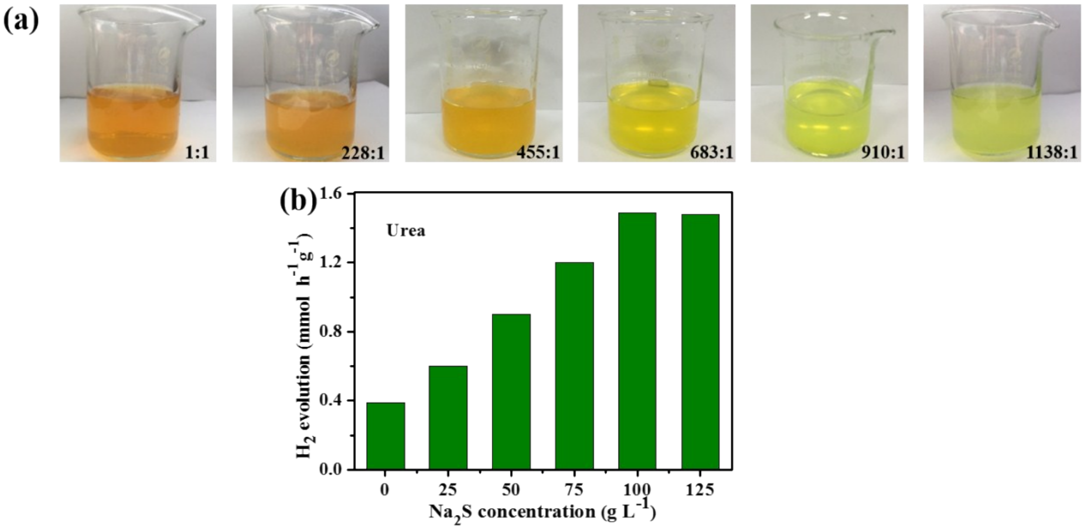

Fig. S20 (a) Digital photographs of CdS_xO product solutions with different ratio of S to Cd ion sources. (b) Photocatalytic H_2 evolution activities for above different CdS_xO products as catalysts in urea solution under simulated 1 sun irradiation.

As the ratio of S to Cd ions in synthetic precursor solutions increases, the product solutions appear different colors varying from reddish brown to yellow green. Based on the photocatalytic performance maximum, the optimum CdS_xO catalyst was selected with the ratio of S to Cd ions at 910 : 1, and the corresponding resultant solution is bright yellow in color.

Table S2. Comparison of various superior photocatalysts recently reported in the literatures for solar H_2 evolution with/without sacrificial agents.

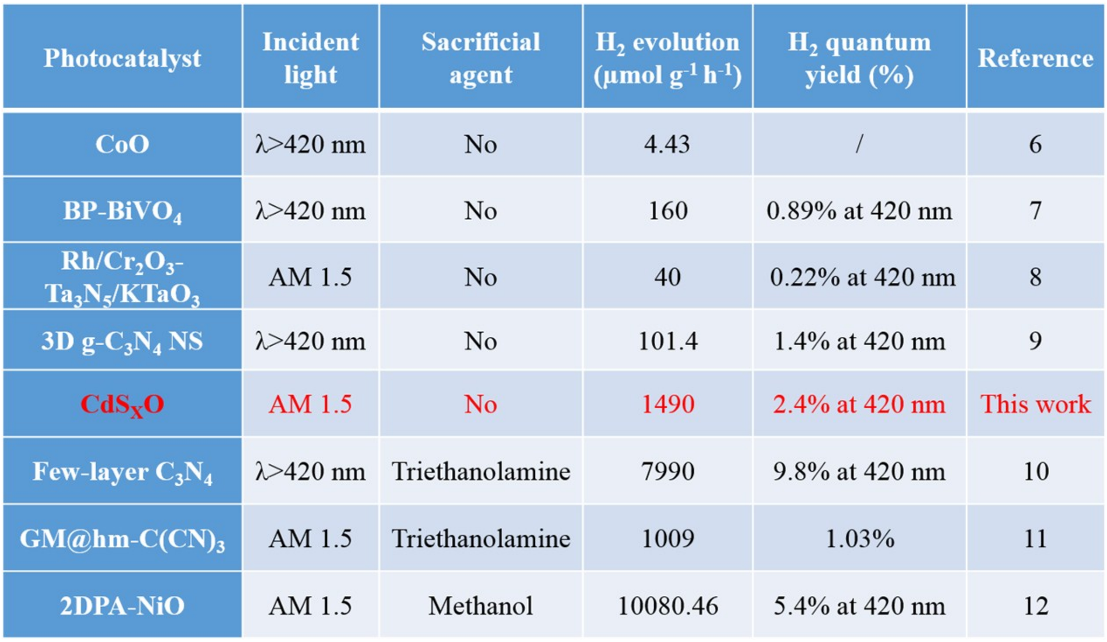

Photocatalyst	Incident light	Sacrificial agent	H_2 evolution (μmol g^{-1} h^{-1})	H_2 quantum yield (%)	Reference
CoO	λ>420 nm	No	4.43	/	6
BP-$BiVO_4$	λ>420 nm	No	160	0.89% at 420 nm	7
Rh/Cr_2O_3-Ta_3N_5/$KTaO_3$	AM 1.5	No	40	0.22% at 420 nm	8
3D g-C_3N_4 NS	λ>420 nm	No	101.4	1.4% at 420 nm	9
CdS_XO	AM 1.5	No	1490	2.4% at 420 nm	This work
Few-layer C_3N_4	λ>420 nm	Triethanolamine	7990	9.8% at 420 nm	10
GM@hm-$C(CN)_3$	AM 1.5	Triethanolamine	1009	1.03%	11
2DPA-NiO	AM 1.5	Methanol	10080.46	5.4% at 420 nm	12

References

1 G. Hodes, I. Howell and L. Peter, *J. Electrochem. Soc.*, 1992, **139**, 3136.

2 X. Zhao, W. Luo, J. Feng, M. Li, Z. Li, T. Yu and Z. Zou, *Adv. Energy Mater.*, 2014, **4**, 1301785.

3 J. M. Catherine, *J. Cluster Sci.*, 1996, **7**, 341.

4 Z. Sun, H. Zheng, J. Li and P. Du, *Energy Environ. Sci.*, 2015, 8, 2668.

5 U. Holzwarth and N. Gibson, *Nat. Nanotech.*, 2011, **6**, 534.

6 J. Xu, X. Li, Z. Ju, Y. Sun, X. Jiao, J. Wu, C. Wang, W. Yan, H. Ju, J. Zhu and Y. Xie, *Angew. Chem. Int. Ed.*, 2019, **131**, 3064.

7 M. Zhu, Z. Sun, M. Fujitsuka and T. Majima, *Angew. Chem. Int. Ed.*, 2018, **57**, 2160.

8 Z. Wang, Y. Inoue, T. Hisatomi, R. Ishikawa, Q. Wang, T. Takata, S. Chen, N. Shibata, Y. Ikuhara and K. Domen, *Nat. Catal.*, 2018, **1**, 756.

9 X. Chen, R. Shi, Q. Chen, Z. Zhang, W. Jiang, Y. Zhu and T.R. Zhang, *Nano Energy*, 2019, **59**, 644.

10 Y. Xiao, G. Tian, W. Li, Y. Xie, B. Jiang, C. Tian, D. Zhao and H. Fu, *J. Am. Chem. Soc.*, 2019, **141**, 2508.

11 G. Zhou, Y. Shan, Y. Hu, X. Xu, L. Long, J. Zhang, J. Dai, J. Guo, J. Shen, S. Li, L. Liu and X. Wu, *Nat. Comm.*, 2018, **9**, 3366.

12 Z. Lin, C. Du, B. Yan, C. Wang and G. Yang, *Nat. Comm.*, 2018, **9**, 4036.